JOURNAL OF SPACECRAFT AND ROCKETS
Vol. 32, No. 2, March–April 1995

Aerodynamic Interference for Supersonic Low-Aspect-Ratio Missiles

H. F. Nelson* and Brent W. Bossi†
University of Missouri—Rolla, Rolla, Missouri 65401

Interference factors $K_{W(B)}$, $K_{B(W)}$, and K_ϕ are used in preliminary design in the equivalent-angle-of-attack method. An Euler code is used to numerically evaluate $K_{W(B)}$, $K_{B(W)}$, and K_ϕ for low-aspect-ratio, cruciform wing–bodies with clipped delta fins for Mach numbers from 3 to 4 and angles of attack up to 20 deg. The ratios of fin span to body radius (S/R) range from 1.3 to 2, so that aspect ratios vary from 0.05 to 4 and taper ratios vary from 0 to 0.975. Euler results compare well with experimental data. At low angle of attack $K_{W(B)}$ is of the order of 1.5 for low-aspect-ratio fins. $K_{W(B)}$ decreases as the angle of attack increases and can be less than 1 at large angles of attack. Shock and expansion waves from the fin interact with the body and strongly influence $K_{B(W)}$. The afterbody length beyond the fin trailing edge also contributes to $K_{B(W)}$. As the aspect ratio decreases from 4 to 0.05, $K_{B(W)}$ increases to a maximum value and then 1) decreases for small angles of attack and 2) remains fairly constant for large angles of attack. K_ϕ is calculated for sideslip angles of ±3 deg. Euler predictions of K_ϕ are larger than slender-body predictions, because of vortex effects. K_ϕ is also influenced by shock and expansion waves from adjacent fins. At small angles of attack K_ϕ is larger for negative sideslip than it is for positive sideslip. At large angles of attack K_ϕ becomes independent of the sign of sideslip angle.

Nomenclature

AR = aspect ratio of wing formed by joining two fins
$C_{N(\mathrm{LPT})}$ = linearized-potential-theory normal-force coefficient (see Appendix)
C_N = wing–body normal-force coefficient
$C_{N,B}$ = body-alone normal-force coefficient
$C_{N,W}$ = fin-alone normal-force coefficient
$C_{N,W(B)}$ = normal-force coefficient on fin in presence of body
$C_{N,B(W)}$ = increment in normal-force coefficient on body due to fin
$C_{N,\alpha W}$ = normal-force curve slope for fin alone
c_r = root-chord length
c_t = tip-chord length
F32 = wing–body configuration of Ref. 15 ($Z_A/R = 4$, $S/R = 2$, AR = 0.5, and $\lambda = 0.5$)
F33 = wing–body configuration of Ref. 15 ($Z_A/R = 4$, $S/R = 2$, AR = 0.5, and $\lambda = 1.0$)
$K_{B(W)}$ = incremental body–fin interference factor
$K_{W(B)}$ = fin–body interference factor
K_ϕ = sideslip interference factor
L_B = body-alone lift
L_W = fin-alone lift
$L_{B(W)}$ = body lift in presence of fin
$L_{W(B)}$ = fin lift in presence of body
M = freestream Mach number
R = body radius
S = fin span, measured from body centerline
Z = wing–body axial coordinate
Z_A = afterbody length
Z_{BL} = body length
Z_{LE} = Z location of fin leading-edge
Z_{TE} = Z location of fin trailing-edge
Z_N = tangent ogive nose length
α = wing–body angle of attack, deg
α_{eq} = equivalent angle of attack
β = wing–body sideslip angle (positive: wind in along right fin), deg
$\Delta C_{N,W}$ = $C_N - C_{N,B}$; see Eq. (11)
$\Delta L_{B(W)}$ = incremental lift on the body in the presence of the fin
$\Delta\alpha_v$ = vortex contribution to α_{eq}
λ = fin taper ratio
Λ = fin leading-edge sweep angle, 45 deg
ϕ = fin roll angle (positive: right fin down), deg

Received May 9, 1992; revision received Nov. 20, 1993; accepted for publication March 31, 1994.

*Professor of Aerospace Engineering, Thermal Radiative Transfer Group, Department of Mechanical and Aerospace Engineering and Engineering Mechanics. Associate Fellow AIAA.

†Graduate Student, Department of Mechanical and Aerospace Engineering and Engineering Mechanics; currently Engineer, Naval Air Warfare Center–Weapons Division, China Lake, CA 93555. Member AIAA.

Introduction

CURRENT trends in missile design emphasize low-aspect-ratio fins so that missile launchers can be smaller and available launcher volume can be better used. Launch tubes are often grouped together in a checkerboard fashion. Low-aspect-ratio missiles can be efficiently stowed in a launch tube to save space and allow clustering of a number of missiles. The ratio of fin span to body radius (S/R) of the cruciform missiles that fit into square launch tubes is $\sqrt{2}$. Typical S/R values of current missiles range from 2 to 4, so the fins must be folded to fit small launchers. This adds mechanical complexity that is avoided with low-aspect-ratio fins.

Very few aerodynamic data exist for low-aspect-ratio missiles. Nielsen et al.[1] developed a method for calculating aerodynamic characteristics of wing–bodies that includes limited low-aspect-ratio data. Lucero[2,3] developed empirical curves based on Morikawa's[4] interference factors to predict the normal-force coefficient for a variety of low-aspect-ratio wing–body configurations for Mach numbers from 2.5 to 7.7 and for α up to 20 deg. The wing–body configurations were cruciform, generally in the + orientation. Lucero's empirical curves are used for preliminary design and have been added to Missile DATCOM[5]; however, better nonempirical methods are needed to improve and expand the database. Recently, an improved aeroprediction code based on α_{eq} has been developed,[6–8] which uses interference factors $K_{W(B)}$ and $K_{B(W)}$ for pitch-plane calculations for planar and cruciform fins.

The equivalent-angle-of-attack method[9–11] is generally used in conceptual and preliminary design. This method analyzes individual missile components separately and then sums the results together to find the total missile normal-force coefficient. The normal-force coefficient for a wing–body configuration is

$$C_N = C_{N,B} + C_{N,W(B)} + C_{N,B(W)} \tag{1}$$

Interference factors are used to account for the mutual interference

between the missile components. They are included in the definition of the equivalent angle of attack, which can be written as

$$\alpha_{eq} = K_{W(B)}\alpha + \frac{4}{AR}K_\phi \alpha\beta \tag{2}$$

where the terms on the right-hand side represent the effects from body upwash and fin sideslip angle, respectively. Note that vortex interaction affects are not considered. $C_{N,W(B)}$ and $C_{N,B(W)}$ are defined in Ref. 10 as

$$C_{N,W(B)} = C_{N,\alpha W}\alpha_{eq} \tag{3}$$

and

$$C_{N,B(W)} = \frac{K_{B(W)}}{K_{W(B)}}C_{N,\alpha W}\alpha_{eq} \tag{4}$$

in the linear angle-of-attack range. The objective of this research is to evaluate the interference factors $K_{W(B)}$, $K_{B(W)}$, and K_ϕ for low-aspect-ratio missiles.

Interference Factors

$K_{W(B)}$ takes account of body upwash effects on the fin and is defined in Ref. 12 as the ratio of the lift of the fin in the presence of the body to the fin-alone lift:

$$K_{W(B)} = \frac{L_{W(B)}}{L_W} \tag{5}$$

When $K_{W(B)}$ is greater than 1, the body interference is constructive in that the fin generates greater lift in the presence of the body than when it is isolated.

$K_{B(W)}$ is defined in Ref. 12 as

$$K_{B(W)} = \frac{\Delta L_{B(W)}}{L_W} = \frac{L_{B(W)} - L_B}{L_W} \tag{6}$$

where $\Delta L_{B(W)}$ is the incremental normal force on the body in the presence of the fin. When $K_{B(W)}$ is positive, the fin interference produces a favorable effect on the body lift: the body and fin produce greater lift than the body alone. Likewise, when $K_{B(W)}$ is negative the fin interference is unfavorable.

K_ϕ is the ratio of the incremental change in fin lift due to sideslip in the presence of the body and other fins to the fin-alone lift. At a specified α, K_ϕ is defined in Ref. 12 as

$$K_\phi = \left[\frac{(L_{W(B)})_{\beta\neq 0} - (L_{W(B)})_{\beta=0}}{L_W}\right]_\alpha \frac{AR}{4\beta} \tag{7}$$

where $L_{W(B)}$ is the normal force on the fin in the presence of the body and the other fins. Note that K_ϕ was generated by sideslipping the wing–body instead of rolling it in this research.

$K_{W(B)}$, $K_{B(W)}$, and K_ϕ data are used in preliminary and conceptual design because that allows the use of fin-alone data, which are readily available, to quickly calculate lift in missile design tradeoff studies. There are not many $K_{W(B)}$, $K_{B(W)}$, and K_ϕ data in the literature for low-aspect-ratio missiles. Nielsen[12] developed theoretical $K_{W(B)}$, $K_{B(W)}$, and K_ϕ data using slender-body theory (SBT). The SBT results are only a function of S/R; there is no dependence on M, AR, or α. In addition to being irrotational and isentropic, SBT is derived from linearized potential theory by assuming that the axial-flow derivatives are negligible compared to the crossflow derivatives. These assumptions limit SBT to small α and preclude its modeling of vorticity, shock waves, and expansion waves. The Euler equations model the flowfield much better than SBT, because they are rotational and they model shock and expansion waves.

Experimental values for $K_{W(B)}$ and $K_{B(W)}$ have been developed from the Triservice–NASA Data Base[13,14] for fins with aspect ratios of 0.5, 1, and 2 at taper ratios of 0.0, 0.5, and 1 by Nielsen.[15] Cruciform wing–bodies in the + orientation were considered at α from 0 to 40 deg and Mach numbers from 2.5 to 4.5. Moore et al.[6–8] have developed interference-factor data using this database. Spearman and Trescott[16] made measurements of lift for cruciform wing–bodies for Mach numbers from 1.50 to 4.63. The fin planforms included both delta and rectangular shapes, and some of the data are for low aspect ratios.

Jenn and Nelson[17] performed a numerical analysis using the Euler code SWINT to extend K_ϕ beyond the limits of SBT for wing–body configurations with two, three, four, and six delta fins and found K_ϕ to be a function of M, AR, and α in addition to S/R. They considered wing–bodies with S/R from 1 to 6 and AR from 2.4 to 4; however, they did not use grid clustering, so their numerical results were inaccurate for S/R less than 2.5, because of the small number of grid points on the fins. Instead, they used scaled values of K_ϕ from SBT for S/R less than 2.5.

Extensive numerical calculations of $K_{W(B)}$, $K_{B(W)}$, and K_ϕ have been done at the University of Missouri–Rolla using Euler analysis for supersonic wing–body configurations.[17–22] They have shown $K_{W(B)}$, $K_{B(W)}$, and K_ϕ to be functions of S/R, M, α, body cross-sectional shape, fin planform shape, and fin vertical position. This research used delta fins for AR from 2.4 to 4 at low α. The current research extends these results not only to fins with taper ratios different than zero, but also to low AR and large α.

Methodology

Wing–Body Geometry

The wing–body configuration used for this research is shown in Fig. 1. The wing–body has a tangent ogive nose with $Z_N/R = 6$ and a cylindrical body for $Z/R \geq 6$. It has clipped delta fins in the + cruciform configuration, which are modeled as infinitely thin flat plates with $\Lambda = 45$ deg. The fin root-chord leading edge was located far from the nose ($Z_{LE}/R = 30$) to minimize nose effects. The aspect ratio varied from 4 (with $\lambda = 0$) over the delta fin to as low as 0.05 (with $\lambda = 0.975$) over the clipped delta fin. The fin trailing edge is straight, and its location for a specific AR depends on S/R. For this research the right-hand-side horizontal fin was analyzed.

Aspect ratio was controlled by the root-chord length. The aspect ratio for the small delta-fin portion at the front of the clipped delta fin is given by

$$AR = 4/\tan\Lambda \tag{8}$$

Starting at the rear of the delta fin [$Z/R = Z_{LE}/R + (S/R - 1)\tan\Lambda$], the fin has constant span (S/R). Thus, on marching down the wing–body, the fin area increases while the span remains constant, so that the aspect ratio decreases as a function of Z/R according to

$$AR = \frac{4\left(\frac{S}{R} - 1\right)}{2\left(\frac{Z}{R} - \frac{Z_{LE}}{R}\right) - \left(\frac{S}{R} - 1\right)\tan\Lambda} \tag{9}$$

At the trailing edge of the delta fin Eqs. (8) and (9) give the same value of AR. As Z/R approaches infinity, Eq. (9) shows that AR approaches zero.

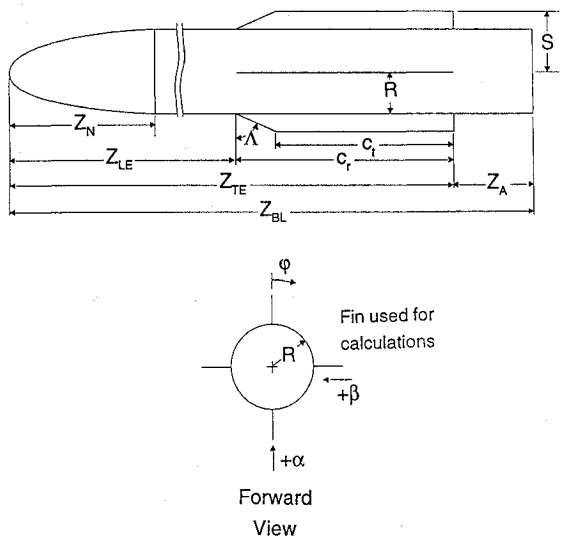

Fig. 1 Missile geometry configuration. The right-hand horizontal fin was used for the calculations. Positive α and β are indicated.

The taper ratio can be expressed in terms of Z/R and S/R, or AR and Λ, as

$$\lambda = 1 - \frac{\left(\frac{S}{R} - 1\right)\tan\Lambda}{\frac{Z}{R} - \frac{Z_{LE}}{R}} = \frac{4 - AR\tan\Lambda}{4 + AR\tan\Lambda} \qquad (10)$$

for $Z/R \geq Z_{LE}/R + (S/R - 1)\tan\Lambda$. The value of λ is zero elsewhere. Thus, AR and λ are related to each other and to Z/R.

The afterbody length is an important parameter for $K_{B(W)}$. Three fins (AR = 0.5, 0.1, and 0.05) were used in the afterbody analysis. For a given Z_{LE}/R, AR, Λ, and S/R, Eq. (9) was used to locate the fin trailing edge. The body was then extended up to 10 body radii beyond the fin trailing edge. This allowed the calculation of $K_{B(W)}$ data in terms of Z_A/R and AR.

ZEUS

The numerical Euler code ZEUS[23–26] (zonal Euler solver) was used for this research. It is a finite-volume code that predicts the steady, supersonic flowfield between the body and the bow shock (used in this research), or between the body and an outer boundary (capturing the bow shock). ZEUS uses a spatial marching method, and the flowfield solution is obtained using the second-order Godunov method in conjuction with the Riemann problem.[27,28] The code is extremely robust and flexible. The ZEUS "velocity-clipping" option was not used in the calculations. The accuracy of ZEUS predictions is documented for a wide spectrum of applications from missiles with noncircular fuselage cross sections to projectiles in tank guns.[20–22,29,30] Many more examples exist, but these references show the versitility of ZEUS.

ZEUS solves the Euler equations to determine the pressure distribution on the missile surface and integrates it over the surface to determine the lift in the presence of the fins. The solution is marched in Z/R along the body, so each step results in a new fin trailing-edge position, or a new, lower AR. Two computer runs are necessary to evaluate $K_{B(W)}$. First, a body-alone analysis is done to find L_B. Next, the wing–body configuration is analyzed to determine $L_{B(W)}$. The difference between these two quantities is $\Delta L_{B(W)}$.

Two computer runs at a given α are needed to calculate K_ϕ: one at $\beta = 0$ deg and one at $\beta = 3$ deg. Each computer run yielded data at slightly different axial locations along the fins. A linear interpolation was used to determine fin forces at 50 identical axial locations for accurate subtraction in Eq. (7) to calculate K_ϕ.

Grid Clustering and Mesh Size

Low-aspect-ratio missiles inherently have small fin spans; consequently, grid clustering is required for accurate numerical results. In this research pitch-plane symmetry was used where possible, and the grid was clustered. A clustering function from Ref. 31 was used, so that at least 10 spanwise grid points were located on the fin trailing edge. ZEUS, as used herein, distributes the grid points between the body and the bow shock. The distance between the body and the bow shock increases as one moves down the body; therefore, this criterion ensured that at least 10 spanwise grid points were located on the fin at every Z/R location. This criterion and ZEUS accuracy were verified in Ref. 32.

The gridding scheme was developed by comparing flowfield predictions using several grid sizes and Courant–Friedrichs–Lewy (CFL) numbers. The CFL number determines the maximum allowable step size for stable solutions. $L_{W(B)}$ predictions using an 18×24 (18 radial points by 24 angular points) uniform grid on the forebody and a 36×36 clustered grid on the finned part of the body, with CFL number 0.9, were compared with predictions using a clustered 72×72 grid and CFL number 0.5. The differences in the results were negligible; consequently, the coarse grid and larger CFL number were used to save computer time.

For $K_{B(W)}$ body-alone calculations at small α, fine grids generated spurious crossflow effects that led to inaccurate body-force predictions.[33] In this research, body-alone results using three mesh sizes (18×24, 36×36, and 36×36 with clustering) were compared with wind-tunnel data, and the coarse mesh gave the best results for long bodies.[34] Consequently, an 18×24 grid mesh was used for the body-alone force predictions.

For K_ϕ calculations pitch-plane symmetry could not be used, and so an 18×48 grid was used on the forebody. A 36×72 grid with radial clustering was used over the fins.

All computer runs were done with CFL number 0.9. The calculations were performed on the IBM 4381 computer at the University of Missouri–Rolla. CPU times up to 2 h were required for complete flowfield solutions over the entire wing–body.

Fin-Alone Lift, L_W

For consistency ZEUS was used to determine L_W, which is presented graphically in the Appendix. Thus, ZEUS is used to predict L_B, $L_{W(B)}$, $L_{B(W)}$, and L_W, which are used to determine $K_{W(B)}$, $K_{B(W)}$, and K_ϕ. The fin-alone ZEUS data agree with the fin-alone data of Ref. 35. In the original AIAA papers in which this work was presented, and in Ref. 34, L_W was generated using linearized potential theory.

Calculation Conditions

$K_{W(B)}$, $K_{B(W)}$, and K_ϕ values are presented for S/R values of 1.3, 1.5, and 2 and aspect ratios from 0.05 to 4 at Mach numbers from 3 to 4. Angles of attack up to 20 deg were investigated in order to examine nonlinear effects of α. All results are for $\Lambda = 45$ deg. The taper ratios ranged from 0 (at AR = 4) to essentially 1 (at AR = 0.05), and they are related to AR by Eq. (10). Care must be taken in using the data because λ changes when AR changes, owing to the geometrical approach used in the analysis; thus the data as a function of AR are also a function of λ. All the graphical data shown are at $M = 3.5$, unless stated otherwise. The data are plotted vs 1/AR, rather than AR, to enhance the low-aspect-ratio regime.

Interference Factor $K_{W(B)}$

Aspect Ratio

Figures 2 and 3 show $K_{W(B)}$ as a function of 1/AR at $M = 3.5$ for $S/R = 1.3$ and 2, respectively. Each figure shows data for $\alpha = 3$, 6, 10, 15, and 20 deg. For $\alpha \leq 10$ deg, $K_{W(B)}$ is greater than 1 for the entire range of AR and S/R. This indicates that the body has a positive effect on fin lift. At $\alpha = 15$ and 20 deg, $K_{W(B)}$ is less than 1 for 1/AR less than about 5, depending upon the value of S/R. The values of $K_{W(B)}$ for $\alpha \geq 15$ deg and 1/AR ≥ 10 (AR ≤ 0.1) are essentially independent of both α and AR.

Figures 2 and 3 include SBT predictions of $K_{W(B)}$ from Ref. 12. The Euler results differ considerably from the SBT predictions. The Euler solutions show that $K_{W(B)}$ decreases with increasing S/R, in agreement with the trends predicted by SBT (compare Figs. 2 and 3). These trends agree with the work of Nielsen,[15] who used experimental data to generate $K_{W(B)}$.

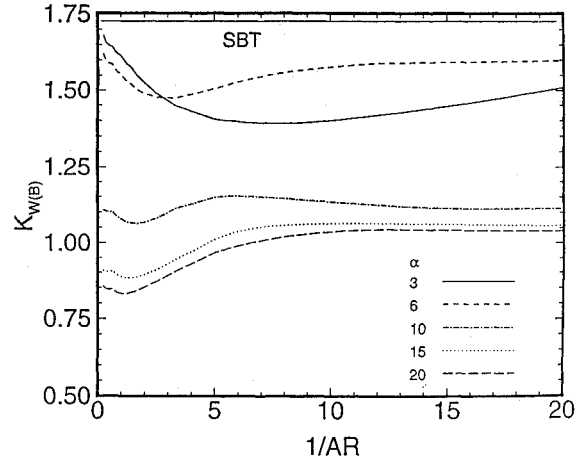

Fig. 2 $K_{W(B)}$ vs 1/AR for $S/R = 1.3$ and $M = 3.5$. The SBT value is 1.745.

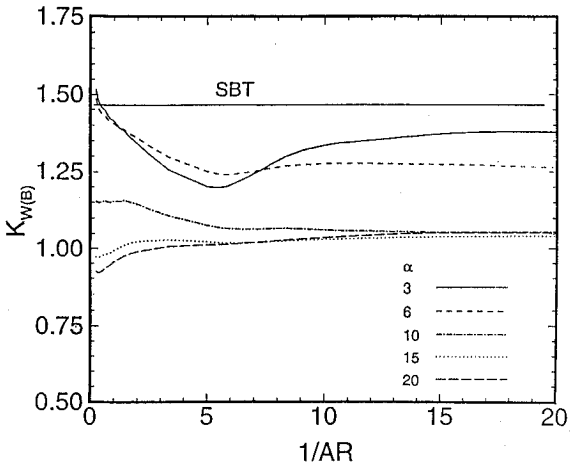

Fig. 3 $K_{W(B)}$ **vs 1/AR for** $S/R = 2$ **and** $M = 3.5$**. The SBT value is 1.450.**

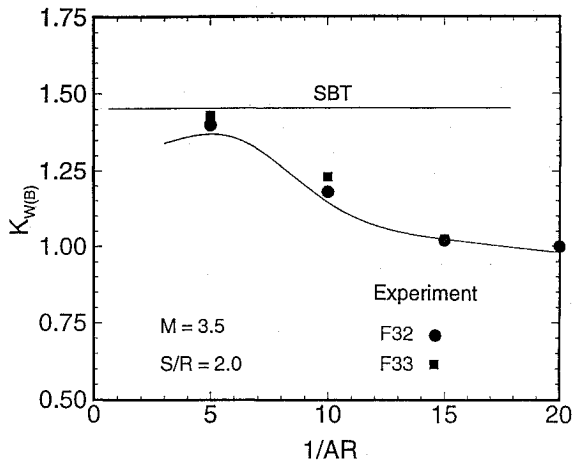

Fig. 4 $K_{W(B)}$ **vs** α **for** $M = 3.5$**, AR = 0.5, and** $S/R = 2$**. Comparison of experiment, SBT, and ZEUS results.**

Angle of Attack

Figure 4 shows $K_{W(B)}$ as a function of α at AR = 0.5 for $S/R = 2$. In general, $K_{W(B)}$ is approximately 1.4 at small α and approaches 1 at large α. The symbols in Fig. 4 show experimental $K_{W(B)}$ data for wing–bodies with AR = 0.5 and $S/R = 2$ for two different fin shapes (fin 32 and fin 33 from Ref. 15). Both fins have finite thickness and $S/R = 2$, but fin 32 has $\lambda = 0.5$, whereas fin 33 has $\lambda = 1$. The taper ratio for the Euler results as calculated here varies with aspect ratio. For $S/R = 2$ and AR = 0.5, Eq. (10) gives $\lambda = 0.778$ for the wing–body used in this research. The three-dimensional Euler results show reasonably good agreement with the experimental data.

Flowfield Analysis

At small α, $K_{W(B)}$ is determined by body upwash, or how the flow in the crossflow plane is altered by the body size and shape. In addition, the shedding of leeside vortices generated from the fin tips affects $K_{W(B)}$ for fins with taper ratios different than 0. The pressure is lowest at the vortex core and increases with distance away from the core; therefore, the vortex increases the lift when it is attached to the fin, because it lowers the leeside pressure. When it detaches, the leeside pressure increases, decreasing the lift. Consequently, the fin-tip vortices significantly affect the fin-alone and the fin-body lift.

For small α and small AR (long root chord), the body upwash and the fin-tip vortices both play a role in $K_{W(B)}$; however, the fin alone only has tip vortices. Body upwash is strongest near the fin root chord. For small AR, the fin root chord is long and the fin-tip vortices for the fin alone and the fin–body become similar; consequently, $K_{W(B)}$ becomes a function only of the body upwash, and its value is directly related to α.

At high α, the leeside vortex is present, but it is highly distorted and thus has a small affect on the leeside pressure distribution. Vortex shedding still occurs as the flow moves down the wing–body; however, the overall nature of the flowfield changes. The fin lift becomes dominated by the flow impacting the bottom surface of the fin, as indicated by large windward pressures and small leeside pressures. The flow changes from a vortex-controlled flowfield to an impact-controlled flowfield near $\alpha = 10$ deg.

Figures 2 and 3 show that $K_{W(B)}$ remains roughly constant and close to 1 for $\alpha \geq 10$ deg for all aspect ratios. This trend can be explained using Newtonian theory. At large α the flow is dominated by the windward pressure, so the body has little effect on $K_{W(B)}$. Newtonian theory for a flat plate shows[36] that the lift increases approximately linearly with α for $15 \leq \alpha \leq 45$ deg. Both the fin alone and the body–fin tend to have this lift variation for large α, so $K_{W(B)}$ tends toward 1.

Interference Factor $K_{B(W)}$

SBT predictions of $K_{B(W)}$ have been presented by Nielsen in Ref. 12, Chap. 5, as 1.39, 1.15, and 0.80 for $S/R = 1.3$, 1.5, and 2, respectively. These predictions of $K_{B(W)}$ are generally much larger than the current Euler results. The only experimental $K_{B(W)}$ values are for wing–bodies with afterbodies.[14,15] Comparisions with experimental data are presented herein for wing–bodies with specific values of Z_A/R. Nelson and Bossi[32] showed that the Euler equations accurately predict $\Delta C_{N,W}$ for nonafterbody wing–bodies. Referring to Eq. (1), $\Delta C_{N,W}$ is defined as

$$\Delta C_{N,W} = C_N - C_{N,B} = C_{N,W(B)} + C_{N,B(W)} \tag{11}$$

where $C_{N,W(B)}$ and $C_{N,B(W)}$ are defined in Eqs. (3) and (4). Equation (11) can be written as

$$\Delta C_{N,W} = C_{N,\alpha W} K_{W(B)} \left(1 + \frac{K_{B(W)}}{K_{W(B)}}\right) \alpha \tag{12}$$

by combining Eqs. (2–4) and (11) when $K_\phi = 0$. Comparisons of the ZEUS-predicted $\Delta C_{N,W}$ were made with wind-tunnel data from Spearman and Trescott,[16] and the differences were found to be below 10%; consequently, the $K_{B(W)}$ predictions should be acceptable for preliminary design.

Aspect Ratio

The $K_{B(W)}$ results are plotted vs 1/AR in Figs. 5 and 6 at $\alpha = 3$, 6, 10, 15, and 20 deg for $S/R = 1.3$, 1.5, and 2, respectively. Figure 6 shows $K_{B(W)}$ at $S/R = 2$. For each α, $K_{B(W)}$ increases with 1/AR until 1/AR = 5 (AR = 0.2). As 1/AR increases above 5, $K_{B(W)}$ decreases for small α, whereas at larger α it remains fairly constant. Figure 5 shows the same general trends for $K_{B(W)}$ as Fig. 6 does, except for three differences. First, the peaks in $K_{B(W)}$ shift to larger values of 1/AR. Second, for large α and very small 1/AR, Fig. 5 shows that $K_{B(W)}$ decreases before steadily increasing to its maximum value. Finally, as S/R decreases, the maximum value of $K_{B(W)}$ increases; however, this is due to the normalization of $K_{B(W)}$, not to the flowfield physics. Large-S/R fins 1) have greater effects on the body force and 2) produce larger $\Delta L_{B(W)}$ values than small-S/R

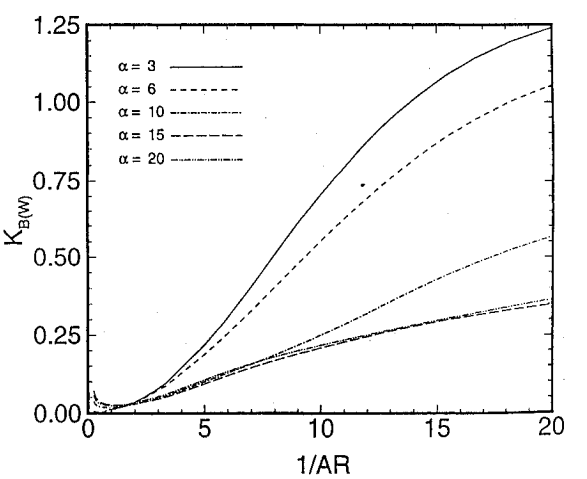

Fig. 5 $K_{B(W)}$ **vs 1/AR for** $S/R = 1.3$ **and** $M = 3.5$**.**

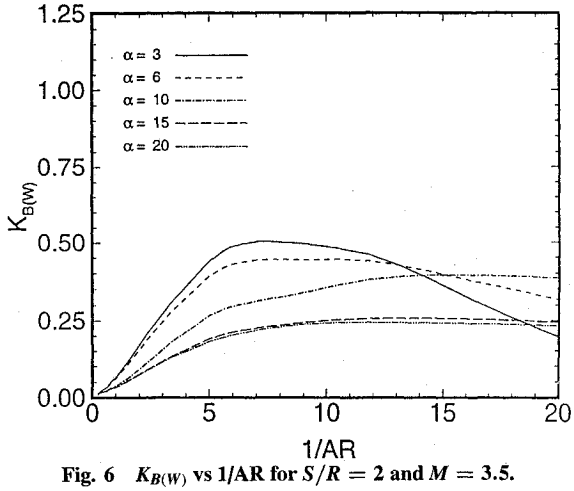

Fig. 6 $K_{B(W)}$ vs 1/AR for $S/R = 2$ and $M = 3.5$.

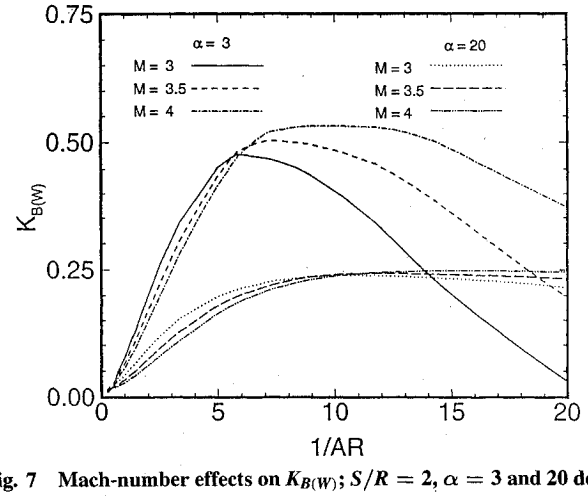

Fig. 7 Mach-number effects on $K_{B(W)}$; $S/R = 2$, $\alpha = 3$ and 20 deg.

fins. Also, when S/R is reduced from 2 to 1.3, $\Delta L_{B(W)}$ decreases less than L_W, leading to larger maximum $K_{B(W)}$. Normalization does not affect $K_{W(B)}$ and K_ϕ, because the numerator deals with fin force and not body force as it does for $K_{B(W)}$. For $K_{W(B)}$ and K_ϕ the fin area cancels, eliminating the sensitivity to normalization [see Eqs. (5) through (7)].

Angle of Attack

Figures 5 and 6 show that $K_{B(W)}$ is a nonlinear function of α at low aspect ratios. At larger aspect ratios (AR $\approx$ 2), $K_{B(W)}$ does not change significantly with α. In addition, $K_{B(W)}$ is more sensitive to changes in angle of attack at small α than at large α. Nielsen found similar trends using experimental data.[15]

Mach Number

Figure 7 shows effects of Mach number on $K_{B(W)}$ as a function of 1/AR at $\alpha = 3$ and 20 deg. As M increases, the maximum value of $K_{B(W)}$ shifts to larger values of 1/AR. At both angles of attack $K_{B(W)}$ decreases with increasing M at low 1/AR and increases with increasing M at large 1/AR. Changing M has a larger effect on $K_{B(W)}$ at low α than at high α.

Afterbody Effects

The ratio Z_A/R represents the extension of the body behind the fin trailing edge and is referred to as the afterbody length. When $Z_A/R = 0$, $K_{B(W)}$ data are generated in terms of AR by marching down the wing–body and using Eq. (9) to convert Z/R to AR. Each new Z/R position represents a new AR. When $Z_A/R > 0$, the fins have a specific AR and trailing-edge location, and the solution is continued for Z/R beyond the fin trailing edge.

Figure 8 shows $K_{B(W)}$ vs Z_A/R for fins with AR = 0.5, 0.1, and 0.05 at $S/R = 2$ and $M = 3.5$, for $\alpha = 10$ and 20 deg. Note that the $K_{B(W)}$ values from Figs. 8 and 6 agree at $Z_A/R = 0$. The large-AR data show a stronger dependence on Z_A/R than the small-AR data.

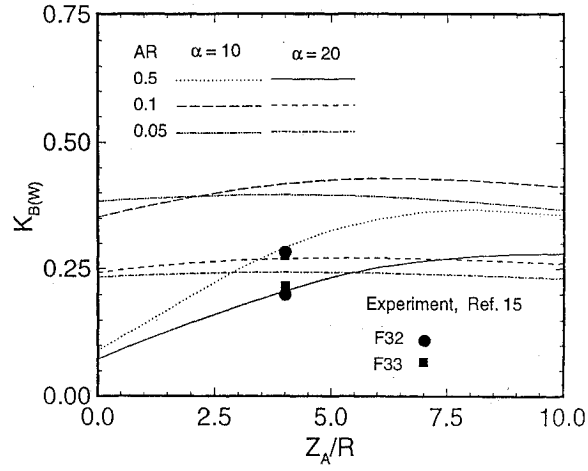

Fig. 8 Afterbody effects, $K_{B(W)}$ vs Z_A/R; $M = 3.5$, $S/R = 2$, $\alpha = 10$ and 20 deg. Experimental $K_{B(W)}$ data are for $Z_A/R = 4$ for F32 at 0.283, and 0.200, and for F33 at 0.276 and 0.216 for $\alpha = 10$ and 20, respectively.

For constant AR, $K_{B(W)}$ initially increases as Z_A/R increases, but reaches a maximum and then decreases slightly. As α increases, the effect of Z_A/R on $K_{B(W)}$ decreases. Nielsen[15] predicted this trend, by generating experimental $K_{B(W)}$ values with the Triservice–NASA Data Base.[13] Data from Table 4 of Ref. 15 for $Z_A/R = 4$, $S/R = 2$, and AR = 0.5, (F32, $\lambda = 0.5$; F33, $\lambda = 1.0$) for $\alpha = 10$ and 20 deg. are presented in Fig. 8. The present results ($\lambda = 0.778$) compare very well with the experimental data, even though the taper ratios do not match.

Flowfield Analysis

The $K_{B(W)}$ data are strongly affected by expansion and shock-wave interaction between the fins and the body. Changes in AR, α, and M directly affect the body pressure distribution, which in turn effects $K_{B(W)}$. An understanding of the pressure distribution is helpful in understanding how AR, α, and M affect $K_{B(W)}$.

On the body at the fin leading edge the pressure above the fin decreases because of the fin expansion wave, while the pressure below the fin increases because of the fin shock wave. The pressure change on the body at larger distances above and below the fin root chord is delayed a short distance downstream from the fin leading edge to where the shock and expansion waves intercept the body. The delay distance is a function not only of the angular position around the body, but also of M and α. Further behind the fin leading edge, the shock and expansion waves entirely intercept the body, and pressure recovery begins to occur. For long wing–bodies pressure recovery occurs along the body. During the pressure recovery $K_{B(W)}$ steadily decreases toward zero for small α. At high α, the shock and expansion waves are stronger and the wave angles rotate relative to the body, thereby delaying pressure recovery and causing the nonlinear behavior of $K_{B(W)}$ as a function of AR and α.

The key elements that determine $K_{B(W)}$ are 1) the strength of the shock and expansion waves, 2) the location where they completely intercept the body, and 3) the body pressure recovery after the shock and expansion waves intercept the body. Each of these three elements is a function of S/R, AR, α, and M.

When S/R decreases, Figs. 5 and 6 show that the maximum values of $K_{B(W)}$ shift to larger values of 1/AR. The shift is a geometry effect based on the relation between AR, S/R, and Z/R given in Eq. (9). Hence, when $K_{B(W)}$ is plotted vs 1/AR, the maximum of each $K_{B(W)}$ curve naturally shifts toward larger 1/AR values as S/R decreases.

Shock and expansion waves are directly responsible for variation of $K_{W(B)}$ with afterbody length. Figure 8 showed that $K_{B(W)}$ changed very little with Z_A/R for wing–bodies with very low-AR fins (AR = 0.05 and 0.1), whereas for wing–bodies with larger-AR fins (AR = 0.5), $K_{B(W)}$ increased as Z_A/R increased. For small-AR wing–bodies the body pressure relaxes to its freestream value at, or prior to, the fin trailing edge, because the fin root chord is long. (For AR = 0.05 and $S/R = 1.3$, the trailing edge is at $Z/R = 42.15$.) For wing–bodies with large-AR fins, the fin root

chord is short, so the fin trailing edge is located close to the fin leading edge. (For AR = 0.5 and $S/R = 1.3$, the trailing edge is at $Z/R = 31.35$.) Consequently, at the fin trailing edge the shock and expansion waves have not completely intercepted the body; hence, they are carried over to the afterbody and cause $K_{B(W)}$ to increase with afterbody length. Once the shock and expansion waves have completely intercepted the body, pressure recovery begins and $K_{B(W)}$ begins to decrease with increasing Z/R.

Interference Factor K_ϕ

An objective of this research was to extend the K_ϕ predictions of Ref. 17 to low AR and higher α. Figure 9 shows a comparison between the clustered ZEUS predictions and the unclustered SWINT–SBT predictions from Ref. 17 for a delta fin wing–body with AR = 2.4. Data on K_ϕ for a two-fin, planar configuration and a four-fin, cruciform configuration are shown. Note that the ZEUS and SWINT predictions of K_ϕ agree well at larger S/R values; however, at low S/R values the ZEUS predictions are much larger than SWINT–SBT predictions. Since low-aspect-ratio missiles generally have small-S/R fins, the large K_ϕ values at small S/R may be extremely important in missile design [see Eq. (2)].

Reference 34 shows that ZEUS predicts accurate flowfields for low-aspect-ratio wing–bodies with S/R values as small as 1.25 when grid clustering is used. The finer mesh more accurately predicts vortex behavior due to the crossflow shockwave, which is primarily responsible for the large K_ϕ values at small S/R. Shock waves are the only source of vorticity for inviscid flow. Recall that SBT does not model vorticity at all. Although the Euler-equation solutions show K_ϕ to increase as S/R is decreased, one expects that there is an S/R value at which K_ϕ reaches a maximum and then decreases. As S/R approaches 1, K_ϕ must approach zero because the fin spans become infinitely small. With this in mind, the K_ϕ curves were faired to zero at $S/R = 1$, starting near $S/R = 1.25$. It is very hard to obtain accurate solutions for S/R less than 1.25.

Vortex effects due to the crossflow shock wave appear to be responsible for the large K_ϕ values at low S/R. The existence of vortices on delta fins is documented by a variety of references for many different situations over a wide range of Mach numbers and angles of attack.[23–25,37,38]

A pressure-difference contour plot was generated to show fin vortex effects on K_ϕ for low-S/R wing–bodies. The pressure-difference contour plot shown in Fig. 10 was generated from four pressure contour plots. They consisted of: 1) the leeward pressure for $\beta = 0$ deg $[(P_{\text{top}})_{\beta=0}]$, 2) the windward pressure for $\beta = 0$ deg $[(P_{\text{bot}})_{\beta=0}]$; 3) the leeward pressure for $\beta = 3$ deg $[(P_{\text{top}})_{\beta=3}]$; and 4) the windward pressure for $\beta = 3$ deg $[(P_{\text{bot}})_{\beta=3}]$. Next, the leeward pressures for $\beta = 0$ deg were subtracted from the leeward pressures for $\beta = 3$ deg. The same was done for the windward pressures. This yields

$$\Delta P_{\text{top}} = (P_{\text{top}})_{\beta=3} - (P_{\text{top}})_{\beta=0} \tag{13}$$

$$\Delta P_{\text{bot}} = (P_{\text{bot}})_{\beta=3} - (P_{\text{bot}})_{\beta=0} \tag{14}$$

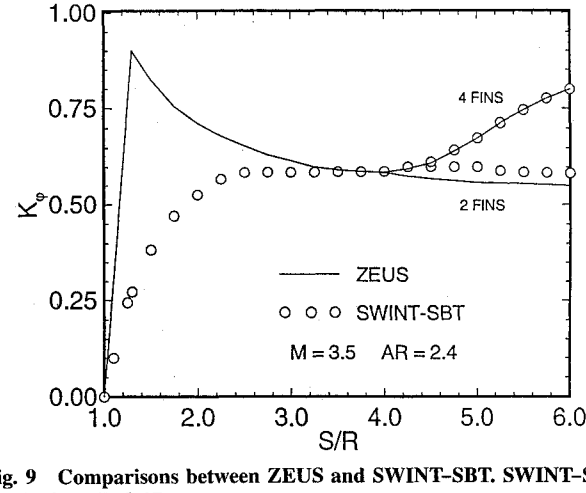

Fig. 9 Comparisons between ZEUS and SWINT-SBT. SWINT-SBT results from Ref. 17.

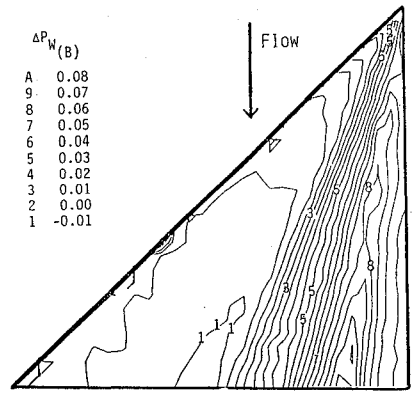

Fig. 10 $\Delta P_{W(B)}$ distribution; AR = 4, $M = 3.5$, $\alpha = 3$ deg, $S/R = 4$.

Next, ΔP_{top} was subtracted from ΔP_{bot}. The resulting quantity is referred to as $\Delta P_{W(B)}$:

$$\Delta P_{W(B)} \equiv \Delta P_{\text{bot}} - \Delta P_{\text{top}} \tag{15}$$

K_ϕ is directly proportional to $\Delta P_{W(B)}$. Figure 10 shows an example of $\Delta P_{W(B)}$ contours. The change in the fin lift in the definition of K_ϕ can be written as

$$\Delta L_{W(B)} = (L_{W(B)})_{\beta\neq 0} - (L_{W(B)})_{\beta=0} \tag{16}$$

The quantity $\Delta L_{W(B)}$ is directly related to the integral of $\Delta P_{W(B)}$ over the fin area.

The distribution of $\Delta P_{W(B)}$ on the fin determines the magnitude of K_ϕ. Figure 10 shows that 1) the largest $\Delta P_{W(B)}$ values occur near the body and decrease as one moves spanwise on the fin, 2) the shock-induced vortex location on the fin acts as a dividing line between the larger and smaller $\Delta P_{W(B)}$ values, and 3) at small S/R, the larger $\Delta P_{W(B)}$ values cover a greater percentage of the fin than at large S/R. The above three observations are the major reasons for the large K_ϕ values for small-S/R wing–bodies. The vortex location determines the percentage of the fin with large $\Delta P_{W(B)}$ values. At small S/R over one-half of the fin is encompassed by large $\Delta P_{W(B)}$ values, which makes K_ϕ large. As S/R is increased, the larger $\Delta P_{W(B)}$ contours cover a smaller percentage of the fin; hence K_ϕ decreases with increasing S/R as shown in Fig. 9.

The above analysis applies directly to low-aspect-ratio fins. Figure 1 shows the generalized low-aspect-ratio wing–body analyzed in this research. Each fin consists of a delta fin at the front. Because of the crossflow shock–vortex interaction, the K_ϕ values on this delta fin are higher than previous SBT predictions, and these large K_ϕ values are carried over to the clipped-delta, low-aspect-ratio fins.

Aspect Ratio

Figures 11 and 12 show K_ϕ vs 1/AR for S/R values of 1.3, 1.5, and 2.0. These figures show that K_ϕ is essentially linear when plotted on log–log scales. Figure 11 shows K_ϕ for $\alpha = 3$ and 20 deg at $\beta = 3$ deg. At small aspect ratios, local maxima occur in the K_ϕ curves for $\alpha = 3$ deg because shock waves from the vertical fins intercept the horizontal fin. This phenomenon was first reported by Jenn and Nelson[17] for larger delta fins. At $\alpha = 20$ deg and $\beta = 3$ deg, the local maxima do not occur, because at high α the shock waves miss the fins. At $\alpha = 20$ deg, K_ϕ is less than it is for $\alpha = 3$ deg. Also, increasing S/R from 1.3 to 2.0 has negligible effect on K_ϕ at $\alpha = 20$ deg.

Figure 12 shows the same type of K_ϕ data as Fig. 11 except it is for $\beta = -3$ deg. Comparing the data of Figs. 11 and 12 shows that K_ϕ at $\beta = -3$ deg is larger than K_ϕ at $\beta = 3$ deg for small α. Jenn and Nelson[17] also found K_ϕ to be larger for negative sideslip. The local maxima for negative sideslip are a result of expansion waves instead of shock waves from the vertical fins, in agreement with the previous results of Ref. 17. As expected, the local maxima disappear when $\alpha = 20$ deg. In fact, at $\alpha = 20$ deg the K_ϕ results for $\beta = -3$ deg are almost identical to those for $\beta = 3$ deg.

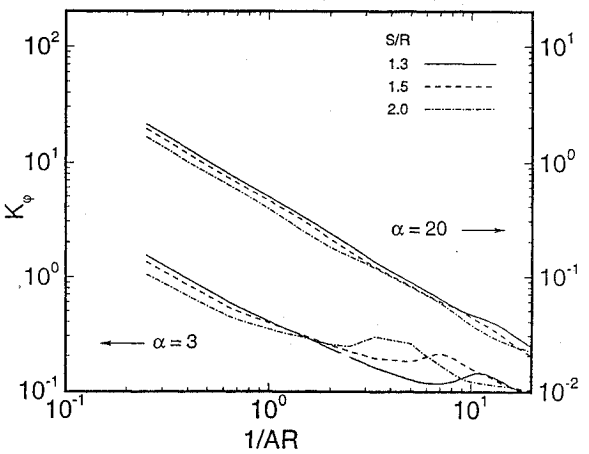

Fig. 11 K_ϕ **vs 1/AR;** $M = 3.5$, $\alpha = 3$ **and 20 deg,** $\beta = 3$ **deg.**

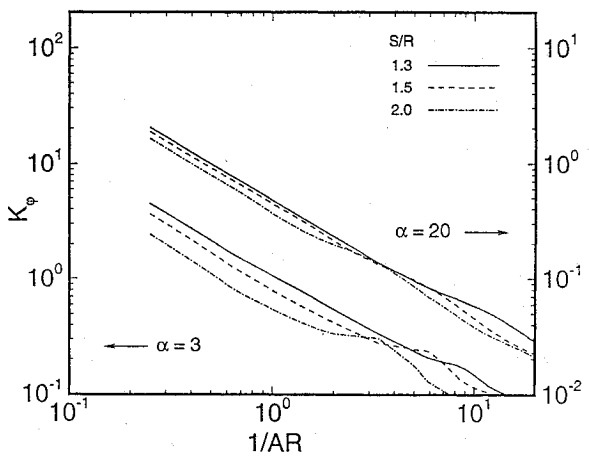

Fig. 12 K_ϕ **vs 1/AR;** $M = 3.5$, $\alpha = 3$ **and 20 deg,** $\beta = -3$ **deg.**

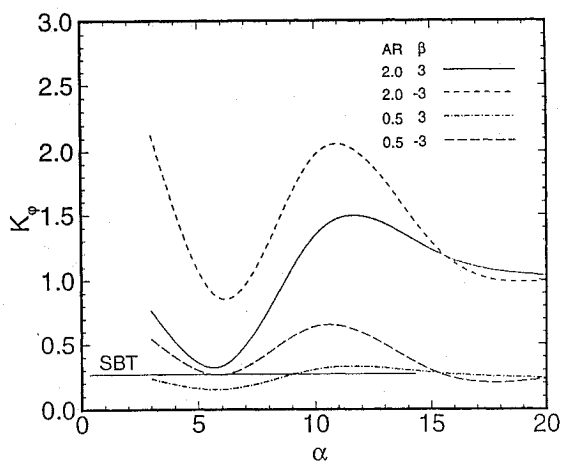

Fig. 13 K_ϕ **vs** α; $M = 3.5$, $S/R = 1.3$, **AR** $= 2$ **and 0.5,** $\beta = \pm 3$ **deg. The SBT value is given by the straight line.**

Angle of Attack

Figures 13 and 14 present K_ϕ vs α at aspect ratios of 2, 0.5, 0.1, and 0.05 for $S/R = 1.3$. These figures show how K_ϕ varies with α. Figure 13 shows K_ϕ data for $\beta = \pm 3$ deg for AR = 2 and 0.5. There is a large dependence on α, especially at negative β. Figure 14 shows K_ϕ data for $\beta = \pm 3$ deg for AR = 0.1 and 0.05. The magnitude of K_ϕ in Fig. 14 is a factor of 10 smaller than for the larger-aspect-ratio wing–bodies of Fig. 13. Comparing the data in Figs. 13 and 14 shows that, in general, K_ϕ becomes more symmetric in β at high α.

Figure 13 also shows the SBT prediction ($K_\phi \approx 0.27$).[12] Recall for SBT that K_ϕ is only a function of S/R, so it does not vary with α. The Euler solutions have extended K_ϕ well beyond the range of SBT for α and AR.

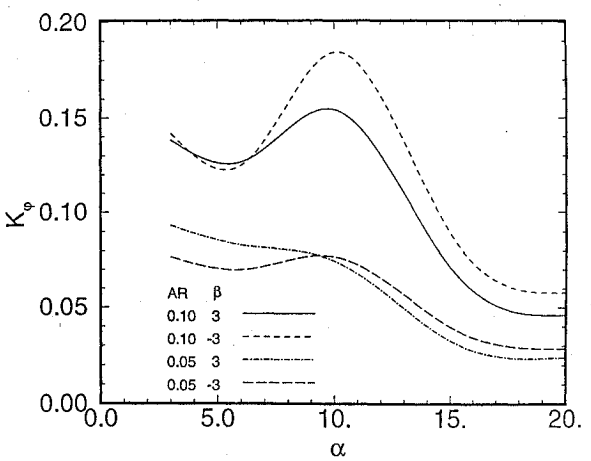

Fig. 14 K_ϕ **vs** α; $M = 3.5$, $S/R = 1.3$, **AR** $= 0.1$ **and 0.05,** $\beta = \pm 3$ **deg.**

Flowfield Analysis

At low angles of attack, portions of the low-aspect-ratio fins are affected by shock and expansion waves from the upper and lower vertical fins (Figs. 11 and 12). In addition, for small-S/R clipped delta fins, K_ϕ is strongly affected by the fin and fin-tip vortices. The wing–body vortices shift as β changes and cover different fractions of the fin planform area, thus influencing $\Delta P_{W(B)}$. The fin-alone lift is always evaluated at $\beta = 0$. These affects are very important at low S/R.

At large α, vortex shedding occurs, but the flowfield becomes Newtonian in nature and the aerodynamic characteristics are dominated by the fluid impacting the bottom surface. This leads to large windward pressures and very low leeward pressures. The pressure distribution becomes independent of the vortex location. The approach to Newtonian-type flow explains why K_ϕ tends to become independent of the sign of β at high α.

For small S/R fins with long root chords, the boundary-layer thickness may become significant and affect $K_{W(B)}$, $K_{B(W)}$, and K_ϕ. A detailed boundary-layer analysis is beyond the scope of this paper. However, a flat-plate analysis (Ref. 36, p. 243) for $M = 3.5$ over an insulated flat wall yields a ratio of boundary-layer thickness to body radius on the fin at its trailing edge on the order of 0.005 to 0.01, depending on aspect ratio. The same magnitude of boundary-layer thickness was found for the body. This estimate implies that effects of boundary-layer thickness on the fin and body are negligible. This analysis was done to obtain the order of magnitudes and does not include high-angle-of-attack or body–fin interaction effects.

Conclusions

The $K_{W(B)}$, $K_{B(W)}$, and K_ϕ predictions presented as a function of AR, α, S/R, and Mach number in this paper extend the conceptual and preliminary design database to low-aspect-ratio supersonic missiles with fins whose taper ratios are greater than 0. For the range of Mach numbers considered herein, there is a nonlinear effect due to the body flow that will affect the interference factors.

Aspect ratio has a significant impact on $K_{W(B)}$. For low α, $K_{W(B)}$ remains greater than 1 over the entire AR range. For large α, $K_{W(B)}$ is less than 1 at large AR and slightly greater than 1 at small AR. The range of AR for which $K_{W(B)}$ is ≤ 1 depends on S/R. The value of $K_{W(B)}$ is insensitive to AR for AR ≤ 0.1 and $\alpha \geq 10$ deg. When $K_{W(B)}$ is less than 1, the fins produce less lift in the presence of the body than when they are isolated, which may detract from the overall missile performance. For large α, $K_{W(B)}$ approaches 1 for all aspect ratios; therefore, the influence of the body on the fin lift becomes less important.

Euler $K_{B(W)}$ values are shown to be much smaller than SBT $K_{B(W)}$ values for low-aspect-ratio wing–bodies. $K_{B(W)}$ was found to be a complicated function of both AR and α. It is strongly dependent on shock- and expansion-wave interference from the fins. For wing–bodies with no afterbody (so that the trailing edge of the fin is at the base of the wing–body) the maximum $K_{B(W)}$ values occur when the combination of S/R and AR is such that the shock and expansion waves from the fin leading edge intercept the entire body

cross section. This occurs at a specific Z/R value. If the wing–body is longer than this Z/R, pressure recovery occurs along the body at small values of α, which tends to decrease $K_{B(W)}$ for the wing–body. At high α the pressure recovery is much slower, because of the Newtonian nature of the flow, and $K_{B(W)}$ remains near its maximum value.

For large-AR wing–bodies, $K_{B(W)}$ varies significantly with afterbody length. The afterbody itself does not alter the flowfield enough to change $K_{B(W)}$. The determining factor is the fin root-chord length, which is short for the large-AR fins. The trailing edge of these fins is reached before the shock and expansion waves have completely interacted with the body. Hence, these interactions are carried over to the afterbody and affect $K_{B(W)}$.

For small-S/R delta fins, the Euler solutions show that K_ϕ is much larger than previous predictions using SBT. The increase in K_ϕ is shown to be due to vortices. This research is the first open-literature paper to point out the importance of vortices for K_ϕ.

For low-AR wing–bodies, K_ϕ approaches zero as AR decreases for all α at both positive and negative β. Also, local maxima in K_ϕ occur as a function of AR. They are caused by shock waves (for positive β) and expansion waves (for negative β) from the neighboring vertical fins. These interactions are important at small α and are more pronounced as S/R increases. The shock- and expansion-wave interference is consistent with the findings of Jenn and Nelson,[17] who showed that these interactions increase K_ϕ.

At small α, K_ϕ tends to be unsymmetric with regard to positive and negative sideslip, with negative sideslip producing larger K_ϕ values. For large α, K_ϕ becomes symmetric in the sideslip angle. This finding is new, and it is particularly important for missile roll control.

Much more numerical and experimental research is needed to fully understand the nature of $K_{W(B)}$, $K_{B(W)}$, and K_ϕ. Boundary-layer effects on both the body and the fins need to be examined. The $K_{W(B)}$, $K_{B(W)}$, and K_ϕ data need to be extended to higher α, β and to a wider range of Mach numbers as well as to noncircular fuselage cross sections.

Appendix: Fin-Alone Force Coefficient $C_{N,F}$

Figures A1 and A2 show the fin-alone lift (numerically generated using ZEUS) vs 1/AR at $M = 3.5$ for $\alpha = 3, 6, 10, 15$, and 20 deg for infinitely thin, clipped delta fins with $\Lambda = 45$ deg at $S/R = 1.3$ and 2, respectively. Figure A3 shows the fin-alone lift at $M = 3$ and 4 for $S/R = 2$. The ordinate on the figures is $C_{N,W}/C_{N(\mathrm{LPT})}$, where $C_{N,W}$ is the fin-alone normal-force coefficient ($C_{N,W} = C_{N,\alpha W}\alpha$) and $C_{N(\mathrm{LPT})}$ is the linearized-potential-theory normal-force coefficient. ($C_{N(\mathrm{LPT})} = 4\alpha/\sqrt{M^2 - 1}$). This ratio makes the data fit nicely on the figures. Note that $S/R = 1.3$ implies that the fin root chord is at $S/R = 1$ and that the fin tip is at $S/R = 1.3$. In other words, the fin has a span of $0.3R$. The wing alone is composed of two fins connected at their root chords. To obtain values of $C_{N,W}$ one must multiply the data in the figures by the appropriate value of $C_{N(\mathrm{LPT})}$.

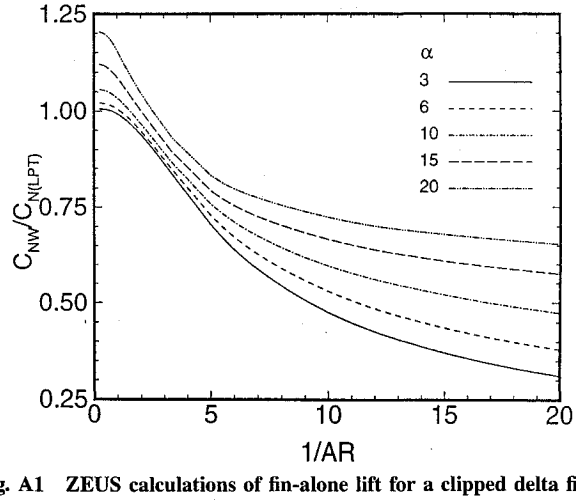

Fig. A1 ZEUS calculations of fin-alone lift for a clipped delta fin at five angles of attack for $S/R = 1.3$ and $M = 3.5$.

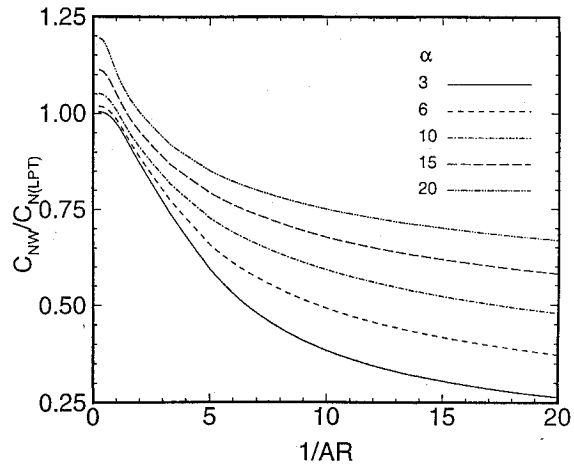

Fig. A2 ZEUS calculations of fin-alone lift for a clipped delta fin at five angles of attack for $S/R = 2$ and $M = 3.5$.

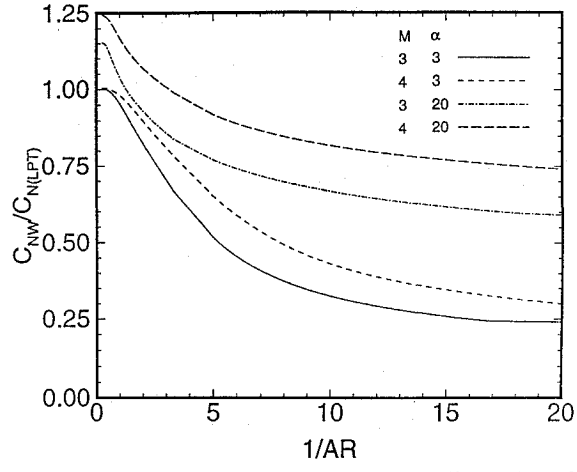

Fig. A3 ZEUS calculations of fin-alone lift for a clipped delta fin at two angles of attack for $S/R = 2$ and $M = 3$ and 4.

The data in these figures show that 1) $C_{N,W}$ is less than $C_{N(\mathrm{LPT})}$ for AR less than about 1, and 2) $C_{N,W}$ falls off as AR decreases. At high AR the Euler-calculated $C_{N,W}$ is higher than $C_{N(\mathrm{LPT})}$ by virtue of the lift enhancement associated with vortex formation along the side edges.

Acknowledgments

This research has been supported by McDonnell Douglas Missile Systems Company, St. Louis, Missouri. Contract monitors were Andrew A. Jenn and Kurt D. Bausch. Additional funds have been provided by the Missouri Research Assistance Act.

References

[1]Nielsen, J. N., Hemsch, M. J., and Smith, C. A., "A Preliminary Method for Calculating the Aerodynamic Characteristics of Cruciform Missiles to High Angles of Attack Including Effects of Roll Angle and Control Deflections," Office of Naval Research, Report ONR-CR215-226-4F, Nov. 1977.

[2]Lucero, E. F., "Approximate Method for Predicting Supersonic Normal-Force Coefficient of Very-Low-Aspect-Ratio Lifting Surfaces," AIAA Paper 84-0575, Jan. 1984.

[3]Lucero, E. F., "Predicting the Supersonic Aerodynamics of Very-Low-Aspect-Ratio Lifting Surfaces," *Journal of Spacecraft and Rockets*, Vol. 22, No. 2, 1985, pp. 119–125.

[4]Morikawa, G., "Supersonic Wing-Body Lift," *Journal of Aeronautical Sciences*, Vol. 18, No. 4, 1951, pp. 217–228.

[5]Bruns, K. D., Moore, M. E., Stoy, S. L., Vukelich, S. R., and Blake, W. B., "MISSILE DATCOM—Revision 4/91," Wright-Patterson Air Force Base, Report WL-TR-91-3039, April 1991.

[6]Moore, F. G., Hymer, T., and Devan, L., "New Methods for Predicting Nonlinear Lift, Center of Pressure, and Pitching Moment on Missile Configurations," Naval Surface Warfare Center, NSWCDD/TR-92/217, July 1992.

[7]Moore, F. G., Hymer, T. C., and Mcinville, R. M., "Improved Aeroprediction Code: Part I—Summary of New Methods and Comparison with Experiment," Naval Surface Warfare Center, NSWCDD/TR-93/91, May 1993.

[8]Moore, F. G., Mcinville, R. M., and Hymer, T. C., "Improved Aeroprediction Code: Part II—Computer Program User's Guide and Listing," Naval Surface Warfare Center, NSWCDD/TR-93/241, Aug. 1993.

[9]Hemsch, M. J., and Nielsen, J. N., "Equivalent Angle-of-Attack Method for Estimating Nonlinear Aerodynamics of Missile Fins," *Journal of Spacecraft and Rockets*, Vol. 20, No. 4, 1993, pp. 356–362.

[10]Hemsch, M. J., "Component Build-Up Method for Engineering Analysis of Missiles at Low-to-High Angles of Attack," *Tactical Missile Aerodynamics: Prediction Methodology*, edited by M. R. Mendenhall, Vol. 142, Progress in Astronautics and Aeronautics, AIAA, Washington, DC, 1992, pp. 115–169.

[11]Hemsch, M. J., and Nielsen, J. N., "Extension of Equivalent Angle-of-Attack Method for Nonlinear Flowfields," *Journal of Spacecraft and Rockets*, Vol. 22, No. 3, 1985, pp. 304–308.

[12]Nielsen, J. N., *Missile Aerodynamics*, McGraw-Hill, New York, 1960; republished by Nielsen Engineering and Research, Mountain View, CA, 1988.

[13]Shaw, D. S., and Sawyer, W. C., "Triservice–NASA Data Base," NASA Langley Research Center, 1991 (unpublished).

[14]Allen, J. M., Shaw, D. S., and Sawyer, W. C., "Analysis of Selected Data from the Triservice Missile Data Base," AIAA Paper 89-0478, Jan. 1989.

[15]Nielsen, J. N., "Supersonic Wing–Body Interference at High Angles of Attack with Emphasis on Low Aspect Ratios," AIAA Paper 86-0568, Jan. 1986.

[16]Spearman, M. L., and Trescott, Jr., C. D., "Effect of Wing Planform on the Static Aerodynamics of a Cruciform Wing–Body Missile for Mach Numbers up to 4.63," NASA TM X-1839, July 1969.

[17]Jenn, A. A., and Nelson, H. F., "Sideslip Effects on Fin–Fin Interference in Supersonic Missile Aerodynamics," *Journal of Spacecraft and Rockets*, Vol. 25, No. 6, 1988, pp. 385–392.

[18]Jenn, A. A., and Nelson, H. F., "Wing Vertical Position Effects on Lift for Supersonic Delta Wing Missiles," *Journal of Spacecraft and Rockets*, Vol. 26, No. 4, 1989, pp. 210–216.

[19]Nelson, H. F., "Wing–Body Interference Lift for Supersonic Missiles with Elliptic Cross-Section Fuselages," *Journal of Spacecraft and Rockets*, Vol. 26, No. 5, 1989, pp. 322–329.

[20]Nelson, H. F., and Talpalliker, M., "Fin–Planform Effects on Lift and Center of Pressure for Supersonic Missiles," *Journal of Spacecraft and Rockets*, Vol. 30, No. 6, 1993, pp. 707–714.

[21]Est, B. E., and Nelson, H. F., "Wing–Body Carryover for Noncircular Missiles," *Journal of Spacecraft and Rockets* (to be published); also AIAA Paper 91-2856, Aug. 1991.

[22]Est, B. E., and Nelson, H. F., "Dihedral Effects on Wing–Body Carryover for Supersonic Noncircular Missiles," *Journal of Spacecraft and Rockets* (to be published); also AIAA Paper 91-3256, Sept. 1991.

[23]Wardlaw, A. B., Jr., and Davis, S. F., "A Second Order Godunov Method for Tactical Missiles," Naval Surface Weapons Center, NSWC TR 86-506, Dec. 1986.

[24]Wardlaw, A. B., Jr., and Priolo, F. J., "Applying the ZEUS Code," Naval Surface Weapons Center, NSWC TR 86-508, Dec. 1986.

[25]Wardlaw, A. B., Jr., Baltakis, F. P., Priolo, F. J., and Solomon, J. M., "Space Marching Euler Methods," *Tactical Missile Aerodynamics: Prediction Methodology*, edited by M. R. Mendenhall, Vol. 142, Progress in Astronautics and Aeronautics, AIAA, Washington, DC, 1992, pp. 379–444.

[26]Glaz, N. M., and Wardlaw, Jr., A. B., "A High-Order Godunov Scheme for Steady Supersonic Gas Dynamics," *Journal of Computational Physics*, Vol. 58, No. 2, 1985, pp. 157–187.

[27]Krispin, J., and Glaz, H. M., "Second Order Godunov Methods and Self-Similar Steady Supersonic Three Dimensional Flowfields," AIAA Paper 91-1653, June 1991.

[28]Osher, S., "Riemann Solvers, the Entropy Condition, and Difference Approximations," *SIAM Journal*, Vol. 21, No. 2, 1984, pp. 217–235.

[29]Evans, J., and Wardlaw, A., "Prediction of Tubular Projectile Aerodynamics Using the ZEUS Euler Code," AIAA Paper 89-0334, Jan. 1989.

[30]Priolo, E. F., and Wardlaw, A. B., Jr., "Euler Space-Marching Computations with Crossflow Separation for Missile-Type Bodies," AIAA Paper 90-0616, Jan. 1990.

[31]Anderson, D. A., Tannehill, J. C., and Pletcher, R. H., *Computational Fluid Mechanics and Heat Transfer*, Hemisphere, New York, 1983, p. 249.

[32]Nelson, H. F., and Bossi, B. W., "Prediction of Low Aspect Ratio Missile Aerodynamics," *Journal of Spacecraft and Rockets* (to be published).

[33]Baltikus, F., private communication, Naval Surface Weapons Center, Silver Spring, MD, Feb. 1990

[34]Bossi, B. W., "Computational Aerodynamics of Low Aspect Ratio Missiles in Supersonic Flow," M.S. Thesis, Dept. of Mechanical and Aerospace Engineering and Engineering Mechanics, Univ. of Missouri–Rolla, MO, Dec. 1991.

[35]Stallings, R. L., Jr., and Lamb, M., "Wing-Alone Aerodynamic Characteristics for High Angles of Attack at Supersonic Speeds," NASA TP 1889, July, 1981.

[36]Anderson, J. D., Jr., *Hypersonic and High Temperature Gas Dynamics*, McGraw-Hill, New York, 1989.

[37]Stallings, R. L., Jr., "Low Aspect Ratio Wings at High Angles of Attack," *Tactical Missile Aerodynamics: General Topics*, edited by M. J. Hemsch, Vol. 141, Progress in Astronautics and Aeronautics, AIAA, Washington, DC, 1992, pp. 251–286.

[38]Miller, D. S., and Wood, R. M., "Leeside Flows over Delta Wings at Supersonic Speeds," *Journal of Aircraft*, Vol. 21, No. 9, 1984, pp. 680–686.

J. M. Allen
Associate Editor